Journal of Materials Science: Materials in Electronics
https://doi.org/10.1007/s10854-019-01352-7

X-ray photoelectron spectroscopy and low temperature Mössbauer study of Ce^{3+} substituted $MnFe_2O_4$

K. Manjunatha[1] · I. C. Sathish[1] · S. P. Kubrin[2] · A. T. Kozakov[2] · T. A. Lastovina[3] · A. V. Nikolskii[2] · K. M. Srinivasamurthy[4] · Mehaboob Pasha[1] · V. Jagadeesha Angadi[1]

Received: 21 February 2019 / Accepted: 15 April 2019

Abstract
Spinel Mn^{2+} $Fe^{3+}_{2-x}Ce^{3+}_{x}O_4$ (where x = 0.01–0.05) polycrystalline nanoparticles were fabricated by solution combustion method using glucose and urea as fuels. X-ray diffractogram (XRD) proved the witness of the cubic crystal consort of products which have the crystallite sizes in between 12 and 8 nm. The size of the sample was accomplished via transmission electron microscopy. The elemental composition of iron and manganese ions valences of $MnCe_xFe_{2-x}O_4$ samples were analyzed by X-ray photoelectron spectroscopy. XPS data reveals iron in all samples was trivalent; manganese was divalent, although tetravalent manganese ions were present on the surface of particles. Magnetic characterization of samples was done via Mössbauer spectroscopy at room temperature and at low temperatures (15 K). The Mössbauer analysis determines the consequence of Ce^{3+} substitution on isomer shift and quadrupole splitting of all samples. The low temperature Mössbauer spectroscopy results indicate that the presence of Ce^{3+} ions in the octahedron sites causes the decrease in the concentration of Fe^{3+} ions.

1 Introduction

Ferrite nanoparticles are emerges as one of the prominent areas cause of its fascinating magnetic behaviour and novel applications [1, 2] in the field of Medical, memory devise, sensor and communication sectors etc. Rare earth (RE) doped ferrite nanoparticles display a promising magnetic properties that are not present in bulk ferrite system. Rare earth substituted spinel ferrites is responsible for remarkable modifications in structure, morphology, electrical and magnetic behaviour of the ferrites [3, 4]. RE elements has larger ionic radius, hence when we substituted into Fe^{3+} site, they may drive the cell symmetry to modified by generating internal stress. As we already know that interactions of Fe–Fe ions govern the magnetic interactions and electrical resistivity of ferrimagnetic materials. Therefore, by addition of RE ions into the spinel crystal lattice, an interaction between Fe–RE ions occurs $3d^5$–$4f^7$ coupling which leads to changes in the structural, microstructural, magnetic and dielectric behavior of the ferrites. The spin–orbit coupling in Mn^{2+} is responsible for generating large magneto-crystalline anisotropy in $MnFe_2O_4$, and $4f^7$ grouped RE ions possess similar spin–orbit coupling. RE^{3+} can be stabilized in B-sites of the $MnFe_2O_4$ crystal lattice and could be responsible for the migration of Mn^{2+} i.e. $3d^7$ ions from the octahedral to the tetrahedral sites with a magnetic moment aligned anti-parallel to those of the RE^{3+} in the spinel lattice. This would be expected to significantly modify the magnetic moment. Furthermore, the anisotropy energy constant and ferrimagnetic ordering temperature of the $MnFe_2O_4$ can be tuned with RE^{3+} substitution. Among the RE^{3+} elements, Cerium ions (Ce^{3+}) possess the magnetic moment of 2.6 μB. However, there are challenging issues the maintenance a single-phase with cubic structure and understanding the magnetic properties. RE ions have a low solubility limit in spinel ferrite and form a secondary orthoferrite-phase $RFeO_3$ beyond their limit. RE ions improve the magnetic properties if they

✉ V. Jagadeesha Angadi
jagadeeshaangadi@presidencyuniversity.in

[1] Department of Physics, School of Engineering, Presidency University, Bengaluru 560064, India

[2] Research Institute of Physics, Southern Federal University, Rostov-on-Don, Russia 344090

[3] International Research Center 'Smart Materials', Southern Federal University, Rostov-on-Don, Russia 344090

[4] Department of Physics, Bangalore University, Bengaluru 560056, India

Published online: 25 April 2019

are accommodated in the spinel lattice whereas the formation of a secondary phase leads to the degradation of the magnetic properties of the materials. Therefore, it is necessary to solubilize the RE ions in the spinel lattice to get the most benefit. According to the literature survey, it can be extracted that very limited literature is available for Cerium doped Mn spinel nanoferrites [5–7]. However, the low temperature magnetic properties was carried out using Mössbauer spectroscopy was not found in the literature. At this juncture, showed a keen interest to report the studies on the structural, and low temperature magnetic properties Ce doped Mn-ferrite prepared by solution combustion route. The main intention to choose $MnFe_2O_4$ is, it was exhibiting stable structure and behaves soft magnetic nature. Site-preference and atomic sizes of dopant can tailor magnetic nature so as to realize its application in high frequency applications.

2 Experimental

The Mn^{2+} $Fe^{3+}_{2-x}Ce^{3+}_{x}O_4$ (where x = 0.01–0.05) powder has been prepared by solution combustion method using stoichiometric amounts of oxidizers and fuel, such as to maintain oxidizers to fuel ratio unity. We take Manganese nitrate Tetra Hydrate ($Mn(NO)_3$ $4H_2O$), Ferric nitrate ($Fe(NO_3)_3$ $9H_2O$) and Cerium nitrate Hexa hydrate ($Ce(NO_3)_3$ $6H_2O$) are used as oxidizers, urea and glucose used as a fuel [8]. The mixture of fuel is taken for increased exothermicity and completion of the reaction, which can be understood on the basis of chemical reactions involved during the process. The metal nitrates and fuels were completely dissolved by using a magnetic stirrer for 1 h, until the formation of homogenous solution. This homogeneous solution was taken in a Pyrex dish and kept in a pre-heated muffle furnace maintained at 450 ± 10 °C. Initially, the solution boiled and subsequently frothed to yield fine powder. The combustion process completed within 20 min. The obtained samples were ground properly and characterized. The structural study were carried out using X-ray diffractometer and the average size was calculated from line broadening of (311) reflection using Debye–Scherrer formula, $S = k\lambda/\beta\cos\theta$ where k = 0.9 is a correction factor to account for the particle shapes, β is the full width at a half maximum (FWHM) of the most intense diffraction peak, λ is the wavelength of X-rays obtained from Cu target = 1.5406 Å and θ is the Bragg's angle. The average particle size is estimated by TEM micrographs using image J software were taken by FETEM with electron energy of 200 kV. The Mössbauer spectra were measured by MS1104Em Mössbauer spectrometer. The ^{57}Co in Rhodium matrix was used as a γ-ray source. The samples were cooled in helium cryostat CCS-850 (Janis Res. Inc., USA). The experimental spectra were fitted using SpectrRelax software [9]. The isomer shifts were calculated with respect to the metallic α-Fe.

3 Result and discussion

3.1 Structural analysis

X-ray diffraction patterns of all samples with chemical formula Mn^{2+} $Fe^{3+}_{2-x}Ce^{3+}_{x}O_4$ (where x = 0.01–0.05) nanoparticles are shown in the Fig. 1. From the XRD results it is observed that, the lattice parameters are found to increase with increasing Ce^{3+} concentration, which is attributed to the fact that the ionic radii of Fe^{3+} (0.63 Å) smaller than that of Ce^{3+} (1.14 Å). The inset of Fig. 1 reveals the shift in the (311) peak position towards higher angles suggests there should be an increase in the crystallite size but the present investigation is attributed as follows. The average crystallite size is found to decrease with increasing Ce^{3+} concentration it was estimated through Scherrer formula [10]. The crystallite size decreases, this is due to the Fe^{3+} is replaced by Ce^{3+} ion which is having larger ionic radii brings lattice distortions results the lesser arrangement of Ce^{3+}–O^{2-} bonds. This inducing a larger crystalline anisotropy and enhances the strain inside the lattice volume. To balance the crystalline anisotropy and strain, the crystallite size gets reduced [11]. The variation of Lattice parameter, crystallite size is as shown in the Table 1. The graphical trend of crystallite size and lattice parameter with Ce^{3+} dopant concentration is depicted in Fig. 2.

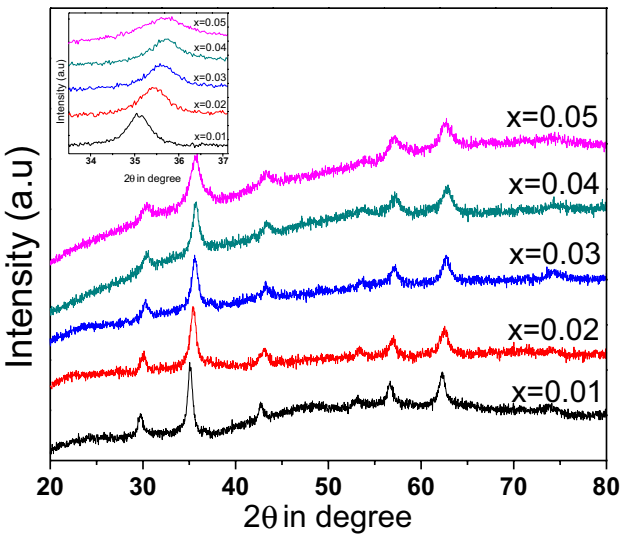

Fig. 1 X-ray diffraction pattern of $MnFe_{2-x}Ce_xO_4$ (x = 0.01–0.05)

Table 1 Shows variation of Lattice parameter (Å), crystallite size (nm) and Internal strain (%) of as synthesized $MnFe_{2-x}Ce_xO_4$ (x = 0.01–0.05) nanoparticles

Composition (x)	Lattice parameter in Å	Crystalite size in nm	Internal strain (%)
0.01	8.3896	12.76	3.527
0.02	8.3919	11.43	3.934
0.03	8.3955	10.71	4.215
0.04	8.4034	9.63	4.692
0.05	8.4078	8.11	5.583

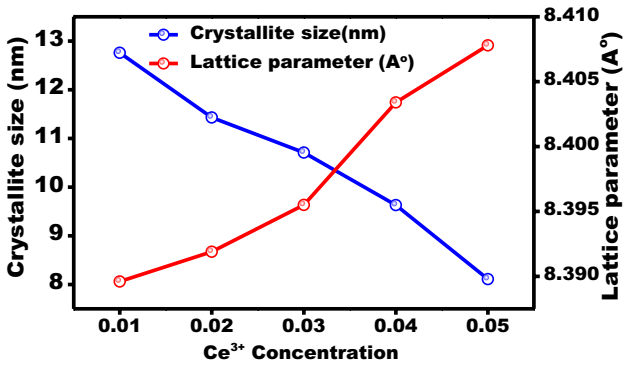

Fig. 2 Variation of Crystallite size (nm) and Lattice parameter (Å) with Ce^{3+} dopant concentration of $MnFe_{2-x}Ce_xO_4$ (x = 0.01–0.05)

3.2 Particle size analysis by TEM micrographs

The TEM micrographs of $MnFe_{2-x}Ce_xO_4$ is depicted in Fig. 3. The particles sizes were measured using "ImageJ" software and the images show spherical particles with less regularity in size and shape. The particles are agglomerated due to their slow growth of the particles during the combustion process. The calculated particle size was about around 20 nm. The particle size obtained from TEM results are in agreements with the average crystallite size calculated by Scherrer formula using XRD data.

3.3 X-ray photoelectron spectroscopy

X-ray photoelectron microprobe (ESCALAB 250X), 500 µm radiation spot on the samples with monochromatic AlK_α radiation line was used for obtaining the chemical shifts of materials. This consists absolute resolved energy interval of 0.6 eV, determined by the $Ag3d_{5/2}$spectral line. The powder samples were deposited on a conductive carbon double sided adhesive tape secured to the metal sample holder. The exposure of low energy electrons was employed to eliminate the positive charge from the sample surface.

Figure 3 shows an overview spectrum of the sample surface with x = 0.05. The carbon content on the surface of samples was quite small. The C1s line with binding energy 285.0 eV was considered to calibrate the energy scale of the spectra. Elemental composition of the sample was determined via a standard method using the relation (1):

$$C_i = \frac{I_i/I_i^\infty}{\sum_{j=1}^{n} I_j/I_j^\infty},$$

here, I_i are the integral intensities of the $Fe2p_{3/2,1/2}$, $Mn2p_{3/2,1/2}$, and O1s XPS lines, and I_i^∞ are Wagner's empirically derived atomic sensitivity factors for XPS [12]. The background was subtracted using Shirley method and the elemental composition was determined using the software kit of the spectrometer. The elemental composition is shown in Table 2. It is seen that for x = 0.01 and 0.02 the elemental composition of the surface approximately corresponds to the expected value. However, there is a substantial segregation of manganese on the surface of nanoparticles at x = 0.03. It should be noted that with increasing x a slight increase of the iron on the surface of nanoparticles was observed. These changes in the composition of manganese and iron occur due to depletion of oxygen on the surface. Small quantity of cerium in the compound is beyond the detection limit of the X-ray photoelectron spectroscopy and it is not detected in the survey spectrum. Therefore, Mn2p-, Fe2p- and O1s spectra were recorded from the samples with x = 0.01–0.05 and the results are shown in Figs. 4 and 5, respectively. The Mn2p spectrum contains spin doublet of $Mn2p_{3/2,1/2}$ in one-electron approximation. The energy positions of both peaks are shown in Table 2. The energy position of $Mn2p_{3/2}$ peak in the energy range 641.8–642.2 can be attributed to Mn^{4+} ion. Perhaps it resides on the surface of the oxide particles in MnO_2 [13]. The energy position of $Mn2p_{3/2}$ peak of 641.2 eV can be attributed to Mn^{2+} in the bulk of the particles [14]. We can assume that the spectra in Fig. 4 are the sum of spectra related to Mn^{2+} and Mn^{4+} ions in the bulk and on the surface of particles, respectively [15]. Figure 3 shows $Fe2p_{3/2,1/2}$ X-ray photoelectron spectra of the samples with x = 0.01–0.05. Similar to the Mn2p spectra, the $Fe2p_{3/2,1/2}$ contains two maximum spectral lines, corresponding to $2p_{3/2}$ and $2p_{1/2}$ energy levels of Fe2p due to spin–orbit coupling. However, $Fe2p_{3/2,1/2}$ spectrum has additional features Sat1 and Sat2, with binding energy of around 719 eV and 733 eV, respectively. These features are called charge transport satellites [16], and they are characteristic of the spectra of samples containing Fe^{3+} ions. Therefore, it should be noted that the iron on the surface of chemical compound have valence of 3^+ state. Figure 4 shows O1s X-ray photoelectron spectra of the samples with x = 0.01–0.05. Despite the fact that the samples were exposed in the air, in the

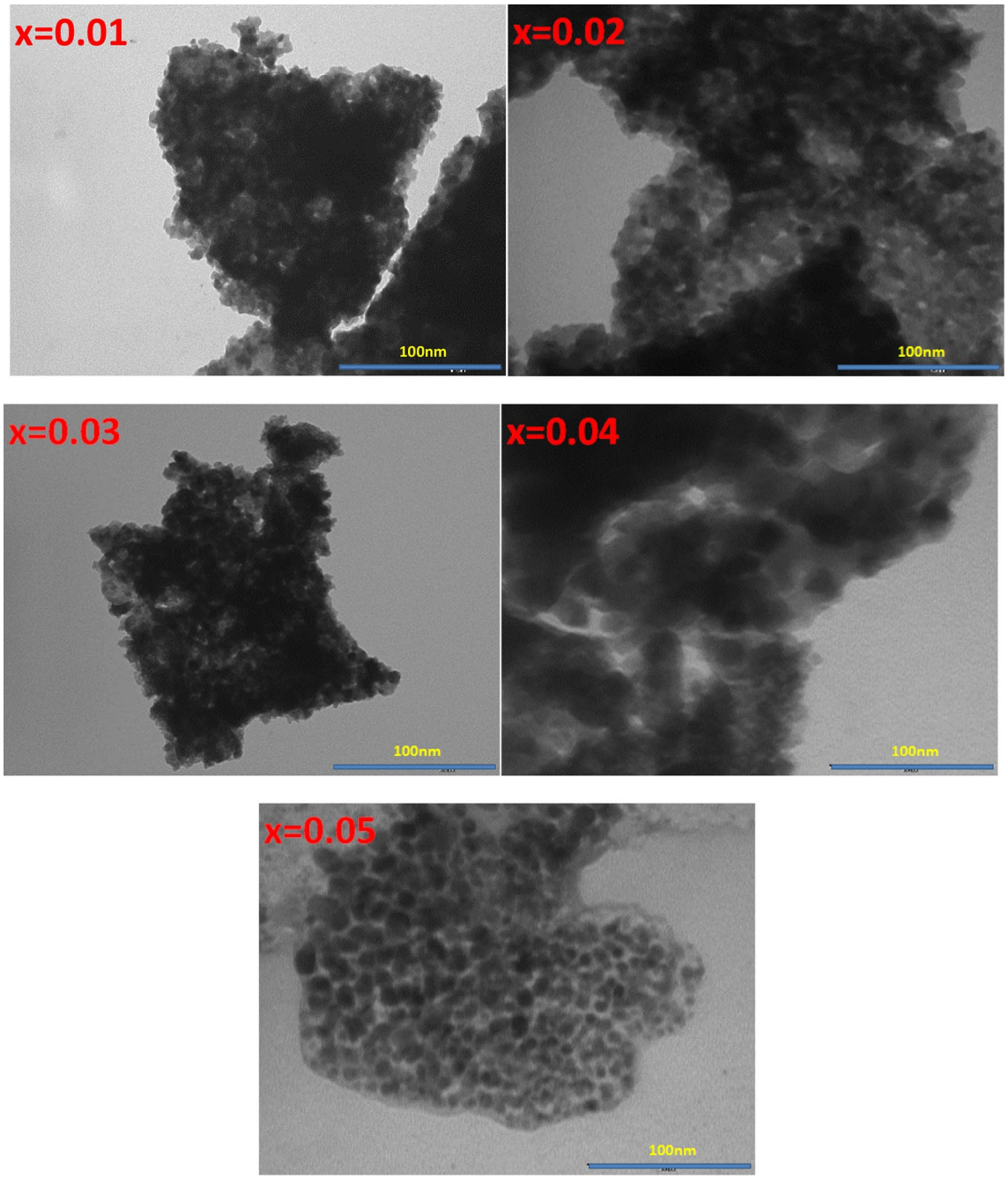

Fig. 3 Transmission Electron microscopy images of $MnFe_{2-x}Ce_xO_4$ (x = 0.01–0.05)

spectra can be easily separated the main peak A of around 530 eV energy (see. Table 3). This peak refers to oxygen belonging to the crystal structure of the samples under study. In addition to the main peak A in the O1s spectra A, B and C peaks are observed. The peak B with the binding energy in the range of 531.7–532.0 eV can be attributed to the hydrocarbon contamination on the surface, the peak C–OH hydroxyl groups or water. Regarding the spectral nature of the A peak it is difficult to predict the chemical state. It can be referred to as a surface contamination and to restoring portion of the particle surface. It is possible to recalculate the elemental composition of the surface of the particles

Table 2 Elemental composition of the samples $MnFe_{2-x}Ce_xO_4$ (x = 0.01, 0.02, 0.03, 0.04, 0.05), at %

x	Mn	Fe	O	Chemical formula of the compound	Notes
0.01	7.3	17.5	75.2	$Mn_{0.5}Fe_{1.2}O_{5.3}$	Withoutcorrection
	8.8	19.5	71.7	$Mn_{0.6}Fe_{1.4}O_{5.0}$	Adjusted for the area of the main peak of A of O1s spectrum
0.02	8.5	20.3	71.20	$Mn_{0.6}Fe_{1.4}O_{5.0}$	Withoutcorrection
	9.6	21.8	68.6	$Mn_{0.7}Fe_{1.5}O_{4.80}$	Adjusted for the area of the main peak of A of O1s spectrum
0.03	18.7	24.2	57.1	$Mn_{1.3}Fe_{1.7}O_{4.0}$	Without correction
	20.1	24.9	55.0	$Mn_{1.4}Fe_{1.7}O_{3.9}$	Adjusted for the area of the main peak of A of O1s spectrum
0.04	19.6	25.6	54.8	$Mn_{1.4}Fe_{1.8}O_{3.8}$	Without correction
	20.3	25.2	54.5	$Mn_{1.4}Fe_{1.8}O_{3.8}$	Adjusted for the area of the main peak of A of O1s spectrum
0.05	19.4	23.9	56.7	$Mn_{1.4}Fe_{1.7}O_{3.9}$	Without correction
	21.5	25.2	53.3	$Mn_{1.5}Fe_{1.8}O_{3.7}$	Adjusted for the area of the main peak of A of O1s spectrum

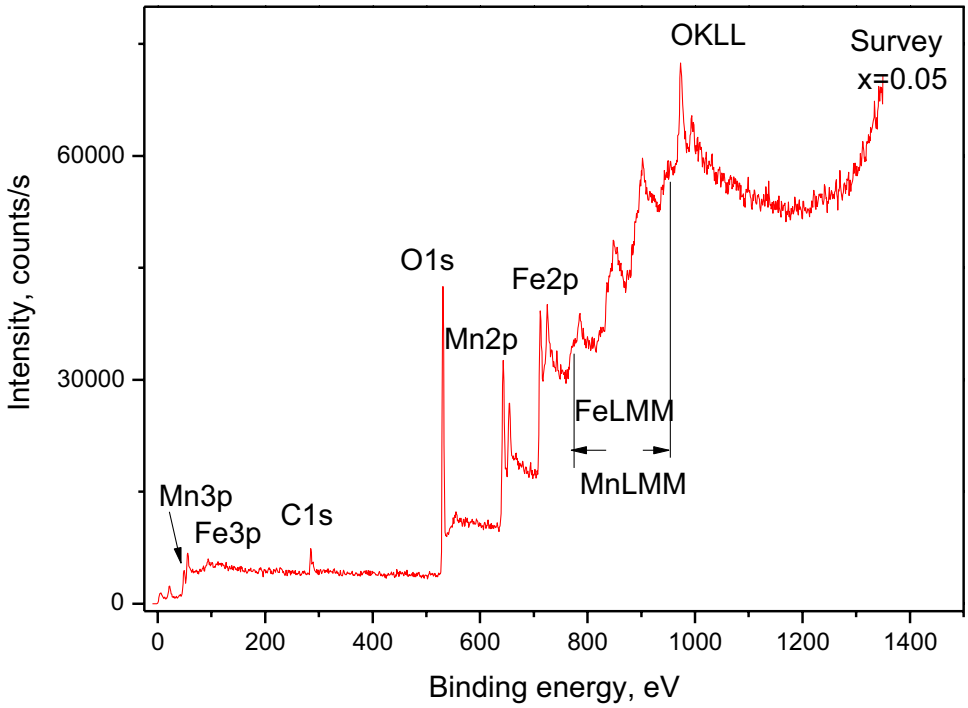

Fig. 4 shows an overview spectrum of the sample surface with x = 0.05

without contamination of the surface, considering area of the major peaks A. This calculated composition is given in each second row of Table 1 for each x.

3.4 Mössbauer spectroscopy analysis

The room temperature Mössbauer spectra are shown in Fig. 6. The spectra consist of asymmetrically broadened Zeeman lines and quadrupole-split lines. The simultaneous presence of a magnetic sextet and a doublet component on the Mössbauer spectra is typical of superparamagnetic nanopowder [17]. The superpamagnetism leads to collapsing of Zeeman structure of Mössbauer spectrum at temperature below T_C. The collapsing occurs when the Mössbauer spectroscopy measuring time (τ_m) which is much shorter than superparamagnetic relaxation time (τ_s) [18]. The temperature, at which the areas of doublet and Zeeman lines are equal, is called the blocking temperature T_B. The T_B value depends on a particle size [19]. The decrease in particle sizes leads to the reduction of T_B. The doublet area values of $MnFe_{2-x}Ce_xO_4$ Mössbauer spectra are ≈ 13% for $x = 0.01$, ≈ 17% for $x = 0.02$ and 0.03, ≈ 23% for $x = 0.04$ and 0.05. These values indicate that T_B is higher than the room temperature, the size of particles for the samples with $x = 0.02$

and 0.03 as well as $x = 0.04$ and 0.05 being close to each other, which is in a good agreement with the XRD particle size data.

The superparamagnetic relaxation leads to asymmetric shape of the lines on the Mössbauer spectra with sharp outer and smeared inward sides [20]. This complicates the model interpretation and reduces the reliability of the Mössbauer spectrum parameters. To minimize the effect of superparamagnetic relaxation the low temperature Mössbauer study was carried out. Figure 7 shows the Mössbauer spectra of $MnFe_{2-x}Ce_xO_4$ nanoparticles taken at 15 K. The spectra consist of three Zeeman sextets with the parameters listed in Table 1. The isomer shift values of sextets are ≈0.45 mm/s and correspond to Fe^{3+} state in the octahedron oxygen environment [21]. The sextet S3 with the lowest effective magnetic field value may be associated with Fe^{3+} ions located in the surface and subsurface layers. The S3 area slightly grows with $x > 0.02$. This indicates that the concentration of Fe^{3+} ions on the surface is increasing. The sextets S1 and S2 seem to correspond to the bulk of the particles. These sextets arise from the two types of octahedrons having different local environment. The area values of S1 and S2 are equal for the samples with x = 0.01 and 0.02. In the samples with x ≥ 0.03 the area of S2 becomes larger than that of S1. Such a redistribution of the areas is the result of ion substitutions of Fe^{3+} by Ce^{3+}.

The effective magnetic field values (H) of Mössbauer spectra of $MnFe_{2-x}Ce_xO_4$ nanoparticles are lower than the observed ones in ferrite spinel ceramics [22]. The reduction of H values is associated with collective magnetic excitations due to superparamagnetic relaxation and can be described by [19, 20, 22]:

$$H(T) = H_0\left(1 - \frac{kT}{KV}\right) \quad (1)$$

where H_0 is hyperfine magnetic field at zero temperature, K is magnetic anisotropy, k is the Boltzmann's constant, T is temperature, V is the volume of particles. The value of H_0 is usually taken as that of the bulk materials.

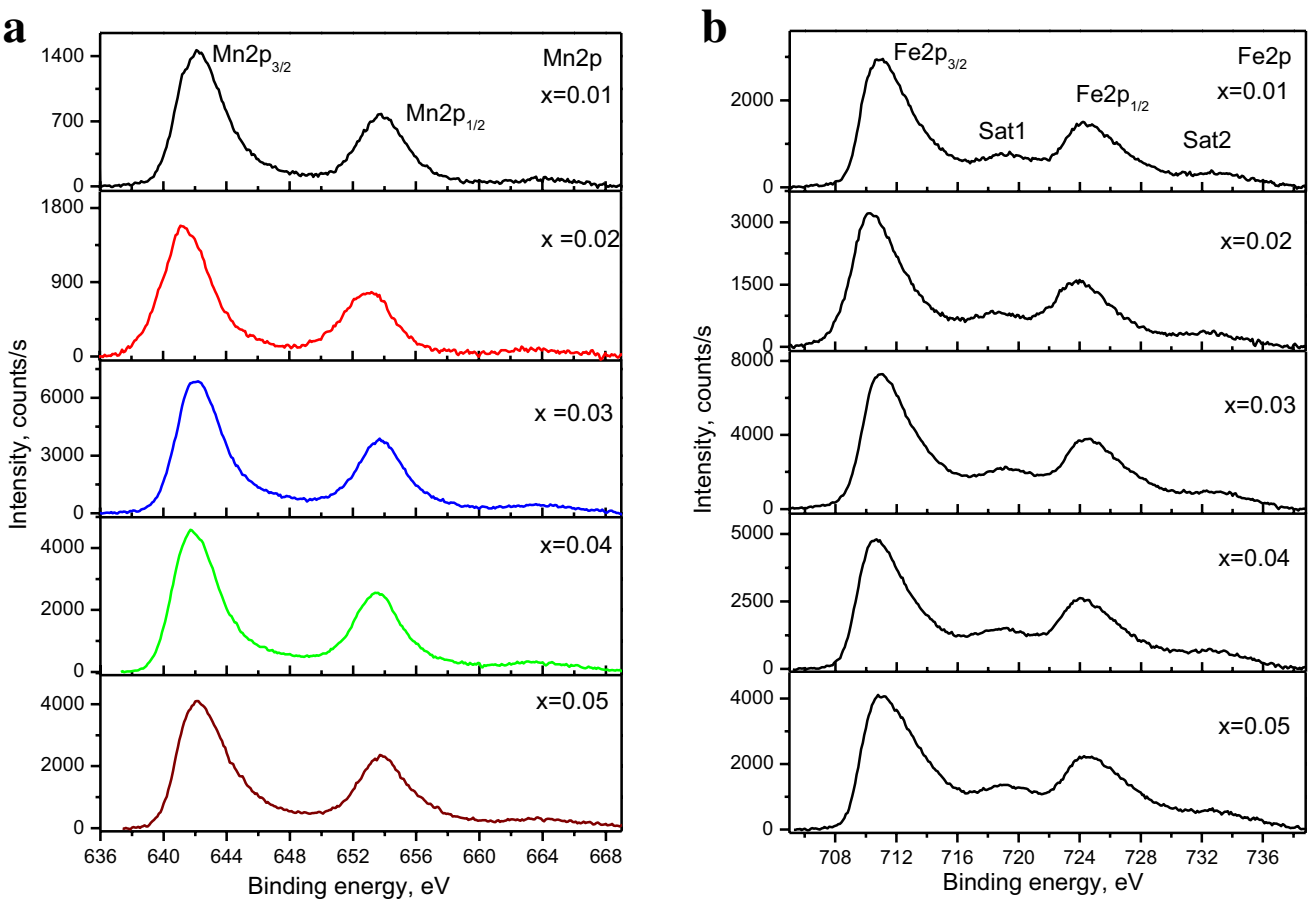

Fig. 5 **a**–**c** represents the Mn2p, Fe2p and O1s spectra of the samples with x = 0.01–0.05 respectively

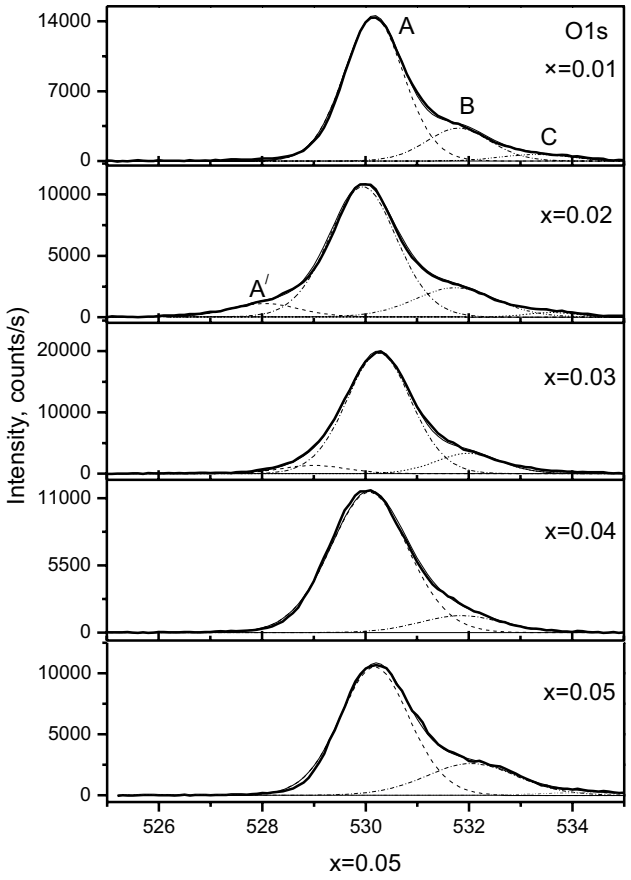

Fig. 5 (continued)

The expression (1) allows one to estimate the K values which are associated with T_B as:

$$T_B = \frac{aKV}{k} \tag{2}$$

where $a = \frac{1}{\ln\left(\frac{\tau_m}{\tau_0}\right)}$.

The calculated values of K and T_B are presented in Table 3. The decrease in particle size of $MnFe_{2-x}Ce_xO_4$ samples lead to regular growthof K values and lowering of T_B values (Tables 4, 5).

4 Conclusions

For the first time, nanocrystalline $MnFe_{2-x}Ce_xO_4$ (x = 0.01–0.05) ferrites have been synthesized successfully by the modified solution combustion. The effect of larger rare-earth Ce^{3+} on the structural, composition and low-temperature Mossbauer spectroscopy of the ferrite samples has been thoroughly investigated. The XRD results reveal that the samples are single-phase and the XRD patterns exhibit spinel cubic structure. The crystallite size decreases with the addition of Ce^{3+} content to the host ferrite, which is in good agreement with the crystallite size obtained from TEM micrographs. The XPS allowed one to explore the elemental composition and iron and manganese ions valences of $MnFe_{2-x}Ce_xO_4$ samples. It has been shown that iron and manganese have Fe^{3+} and Mn^{2+} states, although tetravalent manganese ions were present on the surface of particles. With growing of cerium content, the segregation of manganese and iron on the nanoparticles surface is observed. The room temperature Mössbauer spectra exhibit magnetic sextet and doublet components simultaneously, which suggests that the synthesized material is a superparamagnetic nanopowder. The increasing of doublet area with Ce^{3+}concentration growth indicates that the blocking temperature is above room temperature. The low-temperature Mössbauer spectra have three Zeeman sextets. The isomer shift values of the sextets indicate that Fe^{3+} ions exist in octahedral environments. The redistribution of the sextet area values is the evidence of the substitution of Fe^{3+} by Ce^{3+} at the octahedral sites. The slight increase of the sextet area corresponding to the surface layers with Ce^{3+} concentration is associated with the segregation of iron ions on the surface of $MnFe_{2-x}Ce_xO_4$ nanoparticles. It seems that Ce^{3+}doping leads to the displacement of the Fe^{3+} ions to the nanoparticle surface. There is no monotonous dependence of calculated values of magnetic anisotropy on mean radius of particles probably caused by agglomeration of particles.

Table 3 The binding energy of Mn2p -, Fe2p and O1s—levels in the compounds $MnFe_{2-x}Ce_xO_y$, in eV

x	Mn2p		Fe2p				O1s			
	3/2	1/2	3/2	1/2	Sat1	Sat2	A/	A	B	C
0.01	642.2	653.8	711.0	724.3	719.0	733.3	–	530.2	531.8	533.4
0.02	641.2	653.1	710.4	723.9	718.6	732.0	528.0	530.0	531.7	533.7
0.03	642.0	653.8	711.0	724.5	719.2	732.9	529.0	530.2	532.0	–
0.04	641.8	653.6	710.7	724.0	718.8	732.1	–	530.1	531.9	–
0.05	642.2	653.8	711.0	724.4	719.2	733.0	–	530.2	532.0	534.3

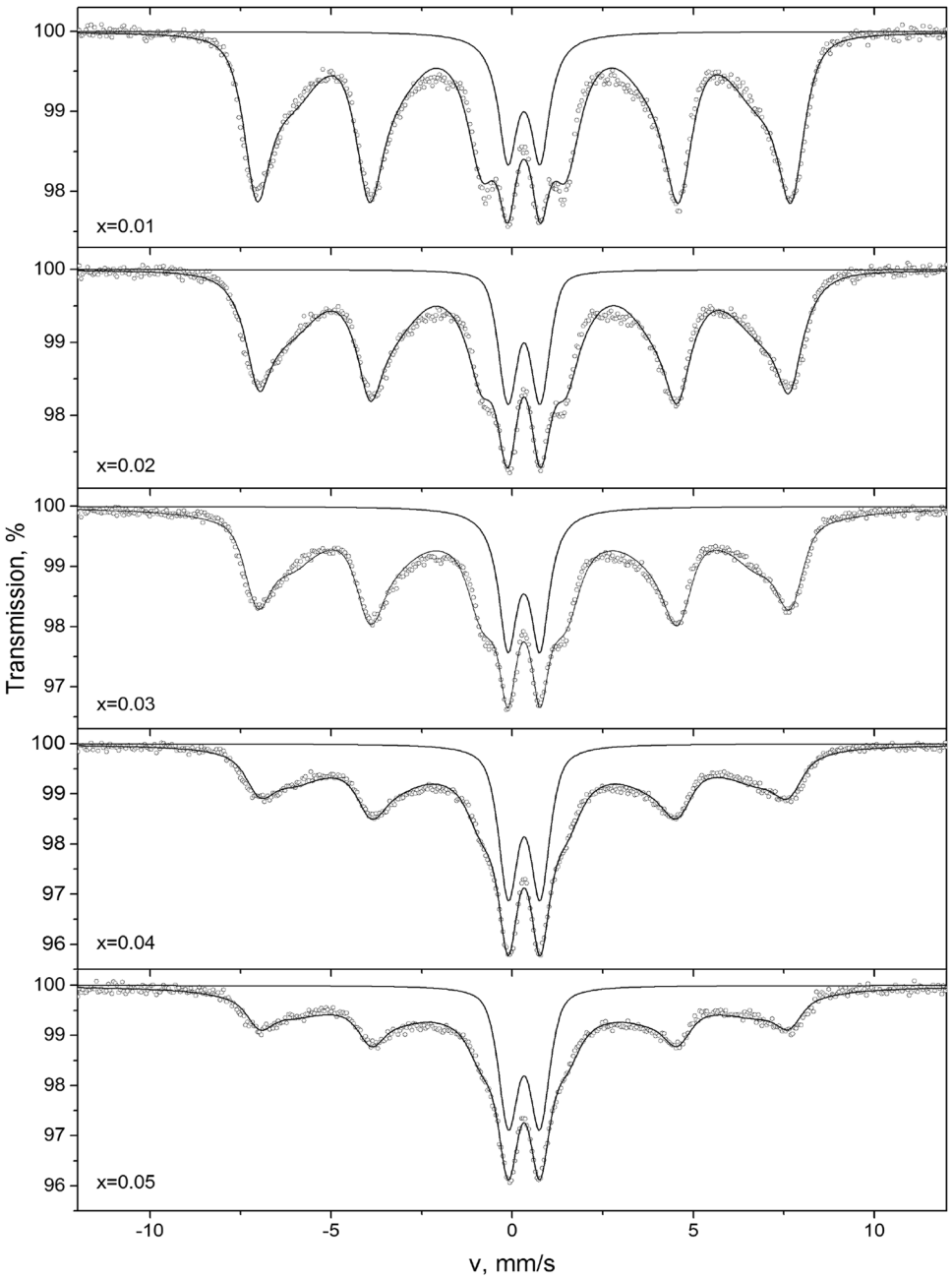

Fig. 6 room temperature Mössbauer spectra of $MnFe_{2-x}Ce_xO_4$ (x = 0.01–0.05)

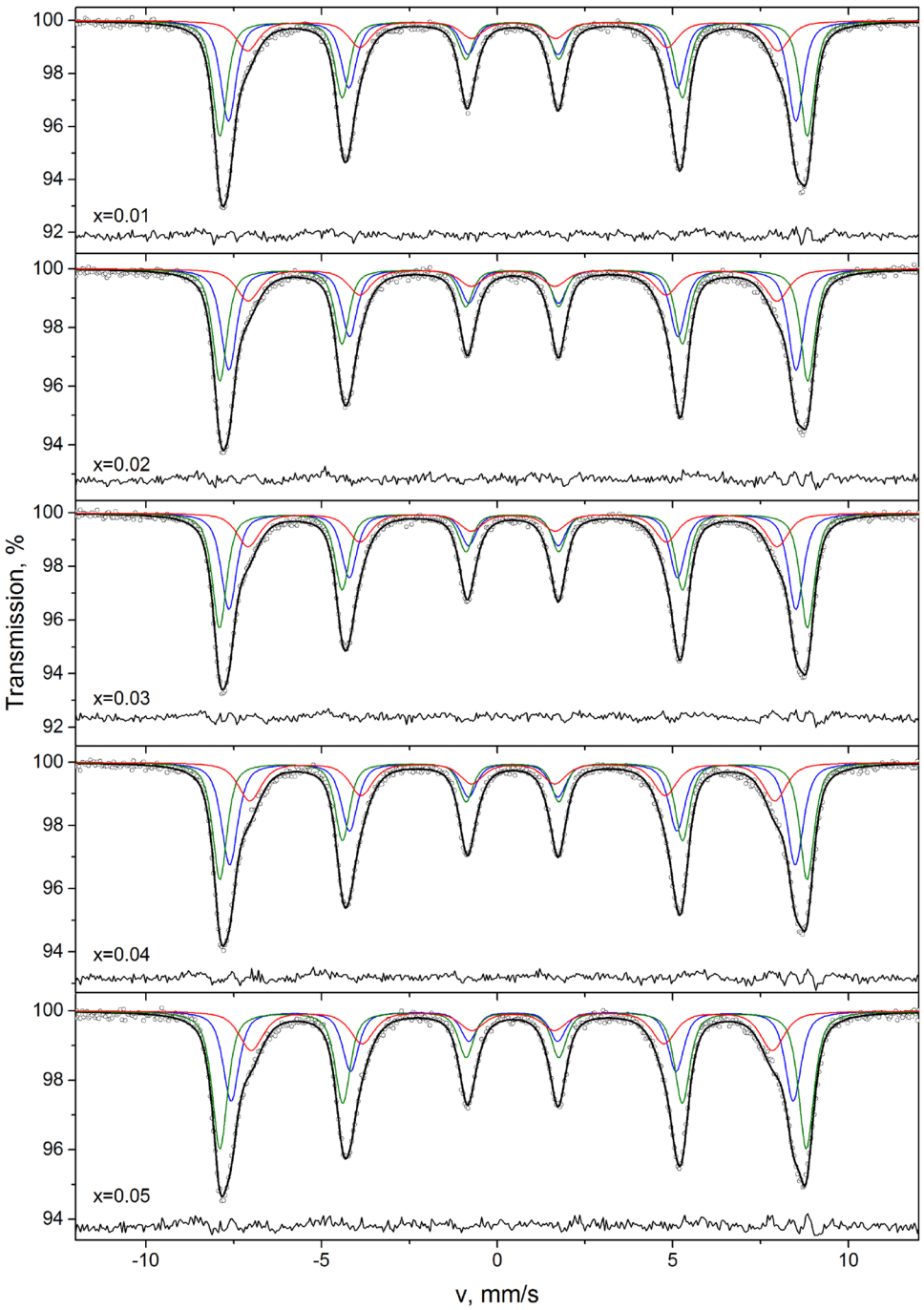

Fig. 7 shows the Mössbauer spectra of $MnFe_{2-x}Ce_xO_4$ nanoparticles taken at 15 K

Table 4 The parameters of $MnFe_{2-x}Ce_xO_4$ nanoparticles Mössbauer spectra taken at 15 K Temperature

x	Component	$\delta \pm 0.02$, mm/s	$\varepsilon \pm 0.02$, mm/s	$H \pm 0.5$, kOe	$G \pm 0.02$, mm/s	$A \pm 1$, %
0.01	S1	0.44	− 0.01	500.9	0.53	39
	S2	0.45	0.02	518.5	0.49	41
	S3	0.46	− 0.01	468.4	0.77	21
0.02	S1	0.45	− 0.02	500.7	0.53	39
	S2	0.45	0.02	518.9	0.49	40
	S3	0.45	− 0.06	466.6	0.80	22
0.03	S1	0.45	− 0.01	500.5	0.52	37
	S2	0.45	0.02	518.9	0.49	41
	S3	0.45	− 0.01	466.9	0.78	22
0.04	S1	0.45	− 0.01	499.2	0.56	38
	S2	0.45	0.01	518.2	0.49	38
	S3	0.44	− 0.01	463.4	0.79	24
0.05	S1	0.44	− 0.02	496.2	0.54	31
	S2	0.44	0.01	517.6	0.52	46
	S3	0.44	− 0.02	460.1	0.82	24

δ isomer shift, ε quadrupole shift, H effective magnetic field on ^{57}Fe nucleus, G spectra line width, A area of spectra component

Table 5 The values of an average radius of nanoparticles r, magnetic anisotropy K and blocking temperature T_B of $Mn_{0.5}Fe_{2-x}Ce_xO_4$samples

x	r, nm	K, J/m^3	T_B, K
0.01	6.0	1.8×10^3	380
0.02	5.0	3.0×10^3	370
0.03	4.5	4.2×10^3	370
0.04	4.0	5.6×10^3	350
0.05	2.5	2.2×10^4	340

Acknowledgements This work was supported by the Ministry of Education and Science of the Russian Federation (Project Nos. 3.6105.2017/8.9, and 3.5346.2017/8.9)

References

1. M. Zheng, X.C. Wu, B.S. Zou, Y.J. Wang, J. Magn. Magn. Mater. **183**, 152 (1998)
2. A.C.F.M. Costa, E. Tortella, M.R. Morelli, R.H.G.A. Kiminami, J. Magn. Magn. Mater. **256**, 174 (2003)
3. A. Verma, T.C. Goel, R.G. Mendiratta, M.I. Alam, Mater. Sci. Eng., B **60**, 156 (1999)
4. N. Rezlescu, E. Rezlescu, D.P. Popa, L. Rezlescu, J. Alloys Comp. **275–277**, 657 (1998)
5. R. Islam, M.A. Hakim, M.O. Rahman, H. Narayan Das, M.A. Mamun, J. Alloys Compd. **559**, 174–180 (2013)
6. Ashok Kumar et al., Ceram. Int. **41**, 1297–1302 (2015)
7. V.J. Angadi, B. Rudraswamy, K. Sadhana, S.R. Murthy, K. Praveena, J. Alloy. Compd. **656**, 5–12 (2016)
8. V.J. Angadi, B. Rudraswamy, K. Sadhana, K. Praveena, J. Magn. Magn. Mater. **409**, 111–115 (2016)
9. M.E. Matsnev, V.S. Rusakov, SpectrRelax: an application for mössbauer spectra modeling and fitting. AIP Conf. Proc. **1489**, 178–185 (2012)
10. K.M. Srinivasamurthy, A.V. Jagadeesha, S.P. Kubrin, S. Matteppanavar, D.A. Sarychev, P. Mohan Kumar, H. Workineh Azale, B. Rudraswamy, Ceram. Int. **44**, 9194–9203 (2018)
11. K.M. Srinivasamurthy, V.J. Angadi, S.P. Kubrin et al., J. Supercond. Nov. Magn. (2018). https://doi.org/10.1007/s10948-018-4752-2
12. D. Briggs, M.P. Seach (eds.), *Practical Surface Analysis by Auger and X-ray Photoelectron Spectroscopy* (Wiley, Chichester, 1983), p. 533
13. A.G. Kochur, A.T. Kozakov, A.V. Nikolskii, K.A. Googlev, A.V. Pavlenko, I.A. Verbenko, L.A. Reznichenko, T.I. Krasnenko, J. Electron Spectrosc. Relat. Phenom. **185**, 175–183 (2012)
14. T. Yamashita, P. Hayes, Analysis of XPS spectra of Fe^{2+} and Fe^{3+} ions in oxide materials. Appl. Surf. Sci. **254**, 2441–2449 (2008)
15. Y.-K. Li, L. Cheng, X.-D. Zhang, X. Guo, Solid State Ion. **336**, 102–109 (2019)
16. S. Nilmoung, P. Kidkhunthod, S. Maensiri, Mater. Chem. Phys. **220**, 190–200 (2018)
17. W. Küdning, H. Bömmel, Some properties of supported small α-Fe_2O_3 particles determined with the mossbauer effect. Phys. Rev. **142**, 327–333 (1966)
18. V.J. Angadi, S.P. Kubrin, D.A. Sarychev, S. Matteppanavar, B. Rudraswamy, H.-L. Liu, K. Praveena, J. Magn. Magn. Mater. **441**, 348–355 (2017)
19. F. Bodker, S. Mørup, Size dependence of the properties of hematite nanoparticles. Europhys. Lett. **52**, 217–223 (2000)
20. M.A. Chuev, On the shape of gamma-resonance spectra of ferrimagnetic nanoparticles under conditions of metamagnetism. JETP Lett. **98**, 465–470 (2013)
21. F. Menil, Systematic trends of the 57Fe mossbauer isomer shifts in (FeO_n) and (FeF_n) polyhedra. Evidence of a new correlation between the isomer shift and the inductive effect of the competing bond T–X (*Fe) (where X is O or F and T any element with a formal positive charge). J. Phys. Chem. Solids **46**, 763–789 (1985)
22. R.E. Vandenberghe, E.D. Grave, Mossbauer effect studies of oxidicspinels, in *Mössbauer Spectroscopy Applied to Inorganic Chemistry*, vol. 3, ed. by G.J. Long, F. Grandjean (Springer, New York, 1989), pp. 59–172